ARCHIVES OF ELECTRICAL ENGINEERING VOL. X(Y), pp. 1-20 (2026)

This paper has been accepted for publication in the AEE journal. This is the version, which has not been fully edited and content may change prior to final publication. Citation information: DOI 10.24425/aee.2026.158267

Influence of step-skew on high-power outer-rotor permanent magnet motors for mining applications

HONGBO QIU, *MIAO LI

College of Building Environment Engineering, Zhengzhou University of Light Industry Zhengzhou city, Henan, China
*e-mail: qiuhongbo@zzuli.edu.cn, *li37853719@163.com*

Abstract: To address the issues of high torque ripple and unstable operation in high-power mining outer-rotor permanent magnet motors (ORPMMs), this study investigates a rotor step-skew technique aimed at enhancing operational smoothness. First, an analytical model of cogging torque that incorporates rotor skew is established based on the energy method, which clarifies the mechanism through which the skew angle influences torque attenuation. From this model, a method for determining the optimal skew angle to minimize cogging torque is derived. Second, a finite element analysis (FEA) model of the ORPMM is constructed to compare electromagnetic characteristics such as no-load back electromotive force (EMF), cogging torque, and torque ripple under both non-skewed and variably skewed rotor conditions. The cogging torque calculated analytically is compared with FEA results, thereby validating the accuracy of the optimal skew angle determination method. Finally, prototype experiments are conducted to verify the accuracy of both the simulation and analytical models. This work provides theoretical foundations and technical support for torque ripple suppression and performance optimization in high-power mining outer-rotor motors.

Key words: analytical calculation, cogging torque, high-power mining outer-rotor permanent magnet motor, step-skew

1. Introduction

High-power outer-rotor permanent magnet motors (ORPMMs) are widely employed in heavy-duty mining applications including coal-mine belt conveyors and hoists, owing to their compact structure, high torque density, and direct-drive capability [1, 2 3]. However, the pursuit of high torque output in such motors is accompanied by notable vibration issues stemming from cogging torque and torque ripple, which significantly degrade operational smoothness and control precision [4]. Compared with inner-rotor counterparts of similar volume, ORPMMs exhibit a larger air-gap circumference, leading to more pronounced magnetic reluctance variations between stator slots and rotor poles. Consequently, their inherent cogging torque and torque ripple are especially acute [5, 6]. Under low-speed, high-torque operating conditions,

This paper has been accepted for publication in the AEE journal. This is the version, which has not been fully edited and content may change prior to final publication. Citation information: DOI 10.24425/aee.2026.158267

these torque-ripple components can be amplified by the mechanical system, further constraining overall equipment performance [7].

To mitigate cogging torque and torque ripple in permanent magnet motors, researchers worldwide propose various methods from multiple perspectives. Scholars Yanbo Lu, Chen Wang, and Jian Huang investigated the phase-shift characteristics, harmonic distribution, and optimization of cogging torque in axial-flux permanent magnet motors using the energy method, a quasi-3D analytical approach, and the frozen-permeability method [8]. Md. Yeasin Arafat, Mahtab Murshed, and Md. Mahamudul Hasan employed analytical models and FEA to study the influence of cogging torque in an outer-rotor radial-flux permanent magnet AC generator under low-speed operation. By deriving an expression for the total cogging torque, they optimized design parameters to reduce its adverse effects on output power quality, vibration, and noise [9]. R. Setiabudy and Herlina explored the impact of the number and width of anti-notches on cogging torque in permanent magnet motors using a notching technique and simulations in FEMM 4.2. Their study found that increasing the number of anti-notches did not significantly improve torque-ripple suppression, whereas a single anti-notch with a specific width delivered the optimal reduction effect [10]. However, these methods often introduce increased manufacturing complexity and can adversely affect the slot fill factor and thermal management.

Ankur Jentibhai Kanapara and Ketan P. Badugjar investigated methods for reducing cogging torque in radial-flux permanent magnet brushless DC motors by modifying the magnet edge margin and slot-opening angle, validating their design through FEA [11]. Amit Kapil and Bhadja Satish employed a magnet edge chamfering technique in the design of a radial-flux PM brushless DC motor and verified its effectiveness in cogging torque reduction using both analytical programming and finite element simulations [12]. M. Tetik Girgin and M. Aydin explored the mitigation of torque ripple in an axial-flux permanent magnet motor through current harmonic injection, implementing a microcontroller-based drive system for experimental validation. Their approach proved effective in suppressing torque ripple, noise, and vibration, though it relies on high-precision sensors and a fast-response controller [13].

However, existing research predominantly focuses on small- to medium-power inner-rotor motors or specific topological structures. A notable lack remains regarding systematic design methodologies and experimental validation regarding segmented skewing for high-power ORPMMs in mining applications. Crucially, a systematic methodology for quantitatively determining the optimal skew angle and a clear understanding of its impact on critical performance indicators, such as back-EMF waveform fidelity, remain lacking for these high-power outer-rotor motors. To address this gap, this study takes a 144-slot/32-pole high-power outer-rotor permanent magnet mining motor as the research object and conducts an optimization study on segmented skewing design. First, an analytical model of cogging torque is established based on the energy method, from which a theoretical expression for the optimal skew angle is derived. The cogging torque calculated by this analytical method is then compared with FEA results. Subsequently, finite element simulations are employed to systematically analyze the motor's no-load back-EMF, cogging torque, and load torque ripple characteristics under different skew angles. Finally, an experimental prototype is developed and tested for validation.

This paper has been accepted for publication in the AEE journal. This is the version, which has not been fully edited and content may change prior to final publication. Citation information: DOI 10.24425/aee.2026.158267

This work provides theoretical foundations and engineering references for the low-vibration, low-noise design of such motors.

2. Motor structure and skewing scheme design

2.1. Research object and basic parameters

This study focuses on a high-power outer-rotor permanent magnet synchronous motor designed for coal mine belt conveyor systems. The motor employs a distributed winding with a short-pitch design with a pitch of 4 to optimize the back-EMF waveform and suppress harmonics. The permanent magnets are surface-mounted on the inner side of the rotor, while the stator is stationary, making it suitable for low-speed, high-torque direct-drive applications. Its key performance and structural parameters are detailed in Table 1.

Table 1. Basic parameters of the motor

Parameters (unit)	**Value**	**Parameters (unit)**	**Value**
Rated power (kW)	315	Rated speed (rpm)	48
Frequency (Hz)	12.8	Air gap length (mm)	2.5
Number of poles	32	Rotor outer diameter (mm)	1220
Axial length (mm)	300	Rotor inner diameter (mm)	1122
Number of slots	144	Stator outer diameter (mm)	1117
Slot opening width (mm)	10.5	Stator inner diameter	903
Slot opening depth (mm)	62.5	Type of circuit	Y

2.2. Finite element modeling

To implement rotor skewing while considering the axial length of the motor, manufacturing feasibility, and optimization efficiency, the rotor was axially divided into eight segments. Within each segment, the permanent magnets retained their original dimensions and magnetization direction, while adjacent segments were offset from each other by a specific mechanical angle in the circumferential direction. This segmented design preserves the inherent advantage of skewing in harmonic suppression while avoiding issues associated with continuous skewing, such as axial magnetic circuit imbalance and complex manufacturing processes. Furthermore, it offers enhanced suitability for the fabrication and assembly of high-power rotors.

To accurately simulate the impact of segmented skewing on motor performance, a three-dimensional 3D FEA model was established based on the parameters listed in Table 1. During mesh generation, local refinement was applied to critical regions including the air gap, permanent magnets, and stator teeth to ensure the accuracy of magnetic field calculations. The resulting 3D FEA model and an unfolded view detailing the local stator-rotor structure are presented in Fig. 1.

This paper has been accepted for publication in the AEE journal. This is the version, which has not been fully edited and content may change prior to final publication. Citation information: DOI 10.24425/aee.2026.158267

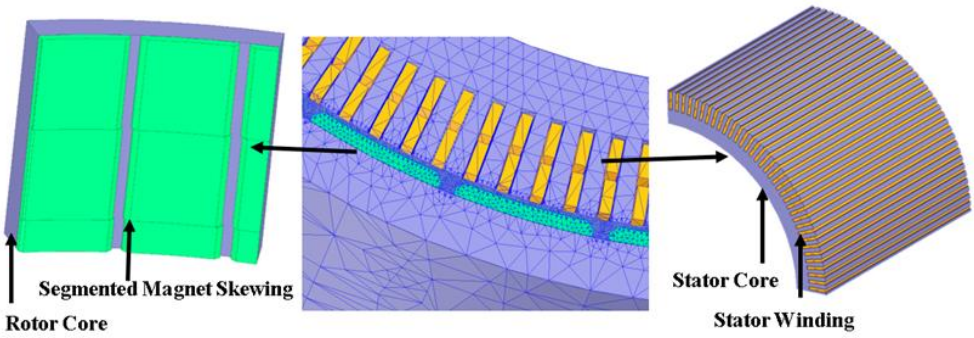

Fig. 1. 3D finite element model and unfolded view of the stator and rotor

3. Analytical calculation of cogging torque and determination of skew angle

To accurately evaluate the influence of segmented rotor skewing on the cogging torque of an outer-rotor motor, the cogging torque is first defined based on the energy method, and the air-gap flux density is decomposed using the permeance method. Building upon this foundation, relevant parameters are determined via a semi-analytical method, leading to the derivation of an analytical expression for the total cogging torque in a non-skewed rotor. This expression is then compared with FEA results. Subsequently, this analytical framework is extended to a skewed rotor structure divided into k segments, where adjacent segments are offset by an angle of $N_s\theta_{s1}$, with N_s representing the number of skewed slots and θ_{s1} denoting the stator slot pitch in radians. The cogging torque for each segment is derived individually, and the total cogging torque for the segmented skewed rotor is obtained by superposition. Finally, to minimize cogging torque, the derived expression is used to solve for the relationship defining the optimal skew angle under different pole-slot combinations and segment numbers.

The magnetic energy stored in the air gap and permanent magnets can be expressed as Eq. (1) [14–18]:

$$W = \frac{1}{2\mu_0}\int_V B^2 \, \mathrm{d}V, \tag{1}$$

where B denotes the air-gap flux density, μ_0 is the permeability of vacuum, and V represents the volume of the air-gap and permanent magnet regions.

The core idea of the permeance method is to decompose the air-gap flux density into the product of the magnetomotive force (MMF) produced by the permanent magnets and the air-gap permeance, as shown in Eq. (2):

$$B(\theta, \alpha) = \Lambda(\theta, \alpha) \cdot F_{\mathrm{PM}}(\theta), \tag{2}$$

This paper has been accepted for publication in the AEE journal. This is the version, which has not been fully edited and content may change prior to final publication. Citation information: DOI 10.24425/aee.2026.158267

where $\Lambda(\theta,\alpha)$ is the air-gap permeance including the permanent magnet region, and $F_{\mathrm{PM}}(\theta)$ is the equivalent MMF produced by the permanent magnets.

Assuming the magnetic permeability of the permanent magnets is equal to that of air, the effective air-gap length is defined as the sum of the permanent magnet thickness and the physical air-gap length, as given by Eq. (3):

$$g_{\mathrm{eff}}(\theta,\alpha) = h_m(\theta) + \delta(\theta,\alpha), \tag{3}$$

where $h_m(\theta)$ denotes the thickness of the permanent magnet, and $\delta(\theta,\alpha)$ represents the actual physical air-gap length.

3.1. Calculation of permanent magnet MMF and air-gap permeance

To establish a slotless structural model based on conditions 1), 2), 3), and 4):

1) A two-dimensional magnetostatic field solver is employed.

2) The inner surface of the stator is simplified as a smooth cylindrical boundary, retaining only the rotor, permanent magnets, and air gap.

3) The material properties of the permanent magnets are defined according to the parameters listed in Table 1, with radial magnetization applied.

4) The air-gap flux density distribution $B_0(\theta)$ within one pole pitch is obtained via FEA. The waveform is subsequently decomposed through Fourier analysis to extract the magnetomotive force harmonic components, as illustrated in Figs. 3(a), 3(b), and 3(c).

The MMF of the permanent magnets is derived from a slotless motor model [19–22]. As illustrated in Fig. 2, for this model, the MMF is expressed as:

$$F_{\mathrm{PM}}(\theta) = \frac{B_0(\theta)(\delta+h_m)}{\mu_0}, \tag{4}$$

where $B_0(\theta)$ is the air-gap flux density distribution when the stator slotting effect is neglected; δ and hm are the air-gap length and the permanent magnet thickness in the slotless model, respectively.

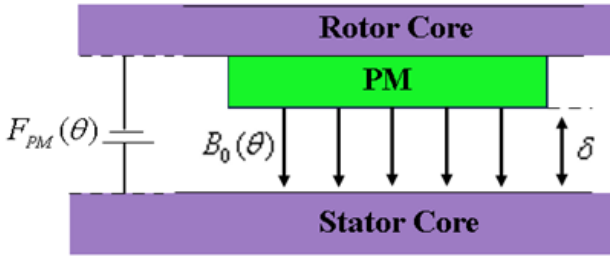

Fig. 2. Slotless model of the motor

The slotless model of the motor is computed using a finite element-based magnetostatic solver to obtain the distribution of the air-gap flux density $B_0(\theta)$, the MMF distribution of the

This paper has been accepted for publication in the AEE journal. This is the version, which has not been fully edited and content may change prior to final publication. Citation information: DOI 10.24425/aee.2026.158267

permanent magnets, and its low-order harmonic components, as shown in Figs. 3(a), 3(b), and 3(c), respectively.

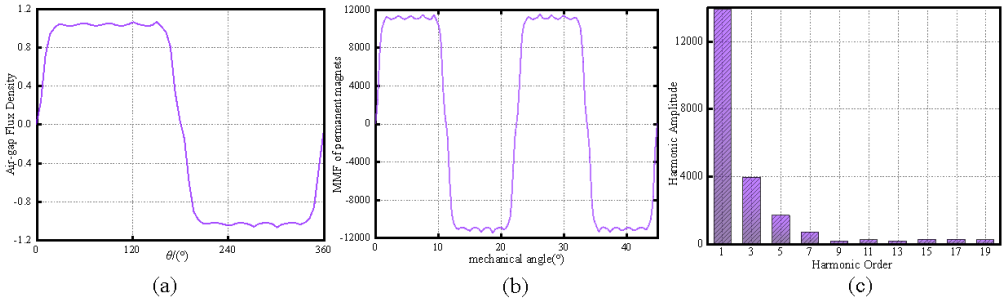

Fig. 3. (a) Distribution of the air-gap flux density $B_0(\theta)$; (b) waveform distribution of permanent magnet MMF; (c) MMF harmonic order

A schematic diagram of a surface-mounted permanent magnet synchronous motor with slotting structure is shown in Fig 4. The MMF $F_{\delta t}$ can be obtained from Eq. (5):

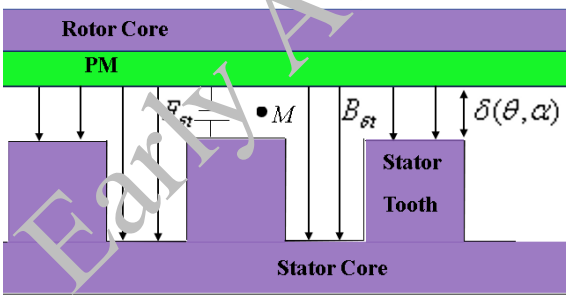

Fig. 4. Schematic of the motor with slotting structure

$$F_{\delta t} = \frac{B_{\delta tM}(\delta(\theta,\alpha)+h_m)}{\mu_0}, \tag{5}$$

where $B_{\delta tM}$ is the flux density at point *M*. Within one stator tooth pitch, the inner surface of the stator can be considered an equipotential magnetic surface. Consequently, the effective air-gap length of the motor can be expressed as:

$$\delta(\theta,\alpha) = \frac{\mu_0 F_{\delta t}}{B_{\delta t}(\theta,\alpha)} - h_m, \tag{6}$$

where $B_{\delta t}(\theta,\alpha)$ is the circumferential distribution of the air-gap flux density over one tooth pitch. The air-gap permeance is therefore:

$$\Lambda(\theta,\alpha) = \frac{\mu_0}{h_m(\theta)+\delta(\theta,\alpha)} = \frac{\mu_0}{h_m}\left[\frac{h_m(\theta)}{h_m(\theta)+\delta(\theta,\alpha)}\right]. \tag{7}$$

This paper has been accepted for publication in the AEE journal. This is the version, which has not been fully edited and content may change prior to final publication. Citation information: DOI 10.24425/aee.2026.158267

For a surface-mounted permanent magnet motor, the equivalent MMF of the permanent magnets can be expressed as:

$$F_{\mathrm{PM}}(\theta) = \frac{B_r(\theta) h_m(\theta)}{\mu_0}, \tag{8}$$

where $B_r(\theta)$ is the circumferential distribution of the permanent magnet remanent flux density.

Furthermore, the differential volume element can be expressed as $\mathrm{d}V = r \cdot \mathrm{d}r \cdot \mathrm{d}\theta \cdot \mathrm{d}z$,with the integration domain corresponding to the air-gap region: radially $r \in [R_1, R_2]$,circumferentially $\theta \in [0,2\pi]$,and axially $z \in [0, L_a]$. In this paper, it is assumed that the effective air-gap length $\delta(\theta, \alpha)$ remains constant along the radial direction—that is, the air-gap magnetic field is uniformly distributed in the radial direction. This assumption is both reasonable and commonly adopted for surface-mounted permanent magnet motors, particularly when the air-gap dimension is considerably smaller than the stator and rotor radii. Consequently, $\delta(\theta, \alpha)$ and the derived permeance function $\Lambda(\theta, \alpha)$ are independent of the radial coordinate r. Under this premise, the radial and axial integrals can be performed first, yielding: $\int_0^{La} \mathrm{d}z = La$, $\int_{R_1}^{R_2} r\,\mathrm{d}r = (R_2^2 - R_1^2)/2$ Substituting these results, together with Eqs. (2), (7), and (8), into Eq. (1), the expression for the magnetic field energy is obtained as Eq. (9):

$$W = \frac{L_a(R_2^2 - R_1^2)}{4\mu_0} \int_0^{2\pi} [\Lambda(\theta, \alpha) F_{\mathrm{PM}}(\theta)]^2 \,\mathrm{d}\theta. \tag{9}$$

The Fourier expansions of the permanent magnet MMF and the air-gap permeance are as follows. The expansion for the square of the MMF is:

$$F_{\mathrm{PM}}^2(\theta) = \frac{h_m^2}{\mu_0^2} B_r^2(\theta) = F_0 + \sum_{m=1}^{\infty} F_m \cos(2mp\theta), \tag{10}$$

where: $F_0 = \frac{h_m^2 \alpha_p B_r^2}{\mu_0^2}$, $F_m = \frac{2h_m^2 B_r^2}{m\pi\mu_0^2} \sin(m\alpha_p \pi)$.

The Fourier expansion for the square of the air-gap permeance is:

$$\Lambda^2(\theta, \alpha) = \frac{\mu_0^2}{h_m^2} [G_0 + \sum_{m=1}^{\infty} G_n \cos[nz(\theta + \alpha)]], \tag{11}$$

where G_0 denotes the constant component of the air-gap permeance, and G_n is the amplitude of the n-th harmonic of the air-gap permeance.

Substituting Eqs. (10) and (11) into Eq. (9) and expanding the four integral components yields Eq. (12):

$$W = \frac{L_a(R_2^2 - R_1^2)}{4\mu_0} \cdot \frac{\mu_0^2}{h_m^2} \int_0^{2\pi} \left[\underbrace{G_0 F_0}_{①} + \underbrace{G_0 \sum_{m=1}^{\infty} F_m \cos(2mp\theta)}_{②} + \underbrace{F_0 \sum_{m=1}^{\infty} G_n \cos[nz(\theta + \alpha)]}_{③} + \underbrace{\sum_{m=1}^{\infty} \sum_{m=1}^{\infty} G_n F_m \cos\big(nz(\theta + \alpha)\big) \cos(2mp\theta)}_{④} \right] \mathrm{d}\theta. \tag{12}$$

The four integral components are evaluated as shown in Eq. (13):

This paper has been accepted for publication in the AEE journal. This is the version, which has not been fully edited and content may change prior to final publication. Citation information: DOI 10.24425/aee.2026.158267

$$\begin{cases} \int_0^{2\pi} G_0 F_0 \mathrm{d}\theta = 2\pi G_0 F_0 \\ \int_0^{2\pi} G_0 \sum_{m=1}^{\infty} F_m \cos(2mp\theta)\mathrm{d}\theta = G_0 \sum_{m=1}^{\infty} F_m \int_0^{2\pi} \cos(2mp\theta)\mathrm{d}\theta = 0, (2mp \neq 0) \\ \int_0^{2\pi} F_0 \sum_{m=1}^{\infty} G_n \cos[nz(\theta+\alpha)]\mathrm{d}\theta = F_0 \sum_{m=1}^{\infty} G_n \int_0^{2\pi} \cos[nz(\theta+\alpha)]\mathrm{d}\theta = 0, (nz \neq 0). \\ \int_0^{2\pi} \cos(nz(\theta+\alpha))\cos(2mp\theta)\mathrm{d}\theta = \begin{cases} \pi\cos \\ 0 \end{cases}(nz\alpha), nz = 2mp \end{cases} \quad (13)$$

Summing the above four integral components and substituting the result back into Eq. (12) yields Eq. (14):

$$W = \frac{\pi L_a (R_2^2 - R_1^2)\mu_0}{4h_m^2}[2G_0F_0 + \sum_{m=1}^{\infty}\sum_{m=1}^{\infty} G_n F_m \cos(nz\alpha)]. \quad (14)$$

Taking the negative partial derivative of Eq. (14) with respect to the position angle α yields the final expression for the cogging torque as Eq. (15):

$$T_{\mathrm{cog}}(\alpha) = \frac{\pi z L_a}{4\mu_0}(R_2^2 - R_1^2)\sum_{n=1}^{\infty} nG_n B_{\frac{nz}{2p}} \sin(nz\alpha), \quad (15)$$

where z is the number of stator slots; L_a is the axial length of the armature; μ_0 is the permeability of free space; R_1 is the outer radius of the stator core; R_2 is the inner radius of the rotor core; N is the integer that makes $nz/(2p)$ an integer; G_n and $B_{nz/(2p)}$ are the Fourier series coefficients of the squared air-gap permeance $\Lambda^2(\theta,\alpha)$ from Eq. (11) and the squared PM MMF $F_{\mathrm{PM}}^2(\theta)$ from Eq. (10), respectively; the term exists when $m = nz/(2p)$ is an integer. Here, n is the summation variable satisfying the condition that $nz/(2p)$ is an integer, and α is the relative angular position between the stator and rotor.

The corresponding Fourier coefficients for the non-skewed rotor, ultimately derived, are listed in Table 2.

Table 2. Calculated Fourier coefficients G_n and B_m

Parameters G_n	Value	Parameters B_m	Value
G_2	1.1809×10^{-6}	B_2	4.2851×10^{2}
G_4	3.7033×10^{-7}	B_4	-2.6998×10^{3}
G_6	3.0620×10^{-7}	B_6	-2.1646×10^{3}
G_8	1.1606×10^{-7}	B_8	1.0452×10^{3}

3.2. Calculation of the optimal skew angle for segmented rotor skewing

For a rotor skewed into k segments, the cogging torques generated by each of the k magnet segments are given respectively as [23–25]:

This paper has been accepted for publication in the AEE journal. This is the version, which has not been fully edited and content may change prior to final publication. Citation information: DOI 10.24425/aee.2026.158267

$$\begin{aligned} T_{\mathrm{cog1}}(\alpha) &= \frac{\pi z L_a}{4\mu_0 k}(R_1^2 - R_2^2)\sum_{n=1}^{\infty} nG_n\, B_{r\frac{nz}{2p}} \sin n\, z\alpha \\ T_{\mathrm{cog2}}(\alpha) &= \frac{\pi z L_a}{4\mu_0 k}(R_1^2 - R_2^2)\sum_{n=1}^{\infty} nG_n\, B_{r\frac{nz}{2p}} \sin n\, z(\alpha + N_s\theta_{s1}) \\ &\vdots \\ T_{\mathrm{cog}k}(\alpha) &= \frac{\pi z L_a}{4\mu_0 k}(R_1^2 - R_2^2)\sum_{n=1}^{\infty} nG_n\, B_{r\frac{nz}{2p}} \sin n\, z[\alpha + (k-1)N_s\theta_{s1}] \end{aligned} . \quad (16)$$

Then, the total cogging torque generated by the *k* magnet segments can be expressed as Eq. (17):

$$T_{\mathrm{cog}}(\alpha) = \sum_{i=1}^{k} T_{\mathrm{cog}i} = \frac{\pi z L_a}{4\mu_0 k}(R_2^2 - R_1^2)\sum_{n=1}^{\infty} nG_n\, B_{\frac{nz}{2p}}\left\{\sum_{i=1}^{k} \sin[nz\alpha + nz(i-1)N_s\theta_{s1}]\right\}. \quad (17)$$

This equation indicates that the total cogging torque after segmented skewing is the vector sum of the cogging torques from each individual segment, and its magnitude depends strongly on the offset angle θ.

When $nN_s \neq 1, 2, 3$

$$T_{\mathrm{cog}}(\alpha) = \frac{\pi z L_a}{4\mu_0 k}(R_2^2 - R_1^2)\sum_{n=1}^{\infty} nG_n\, B_{\frac{nz}{2p}} \frac{\sin\frac{nkzN_s\theta_{s1}}{2}}{\sin\frac{nN_s\theta_{s1}}{2}} \sin\left[nz(\alpha + \tfrac{k-1}{2}N_s\theta_{s1})\right]. \quad (18)$$

To theoretically minimize the cogging torque, setting $\sin\frac{nkzN_s\theta_{s1}}{2} = 0$ enables the cogging torque to be eliminated. Specifically, when n takes its minimum value $N_p = 2p/\,GCD(z, 2p) = 32/GCD(144,32) = 2$, satisfying $\sin\frac{nkzN_s\theta_{s1}}{2} = 0$ ensures that the cogging torque components corresponding to other values of n also vanish. Therefore, the condition for zero cogging torque is given by: $\sin\frac{nkzN_s\theta_{s1}}{2} = 0$ and $\sin\frac{nzN_s\theta_{s1}}{2} \neq 0$. Taking the smallest positive solution yields $\frac{nkzN_s\theta_{s1}}{2} = \pi$, given that $\theta_{s1} = \frac{2\pi}{z} = \frac{360^\circ}{144} = 2.5^\circ$, solving for N_s gives $N_s = \frac{1}{N_p k}$. Accordingly, the mechanical offset angle between adjacent segments is expressed by Eq. (19):

$$\Delta\theta = N_s\theta_{s1} = \frac{1}{kN_p} \cdot \frac{2\pi}{z}. \quad (19)$$

The cumulative mechanical skew angle of the *k*-th permanent magnet segment relative to the first segment can be expressed by Eq. (20):

$$\theta_k = (k-1)\Delta\theta = \frac{k-1}{kN_p}\theta_{s1}. \quad (20)$$

The angle calculated by Eq. (20) represents the theoretical optimal rotor skew angle that minimizes the cogging torque for a given pole-slot combination and number of segments. For the motor under consideration, with the number of segments $k = 8$, $N_p = 2p/\,GCD(z, 2p) = 32/GCD(144,32) = 2$, where $GCD(z, 2p)$ denotes the greatest common divisor of the number of slots z and the number of poles $2p$, and

This paper has been accepted for publication in the AEE journal. This is the version, which has not been fully edited and content may change prior to final publication. Citation information: DOI 10.24425/aee.2026.158267

$\theta_{s1} = \frac{2\pi}{z} = \frac{360^\circ}{144} = 2.5^\circ$. The optimal skew angle is thus obtained as: $\theta_k = \frac{7}{8} \cdot \frac{1}{2} \cdot 2.5^\circ = 1.09375^\circ \approx 1.09^\circ$.

3.3. Analysis of cogging torque

Cogging torque serves as a critical electromagnetic performance metric for permanent magnet motors. Its amplitude directly affects torque ripple, low-speed smoothness, and operational noise, making it a key indicator of overall motor performance. Investigating the variation of cogging torque under different skew angles provides essential guidance for optimizing motor structural parameters and improving operational characteristics.

To this end, three different skew angle schemes are designed to analyze their effects on cogging torque and to validate the rationality of the optimal angle selected in this paper. Among them, the 0° skew angle scheme corresponds to the original structure without rotor skewing, serving as the benchmark scheme; the 1.09° skew angle scheme is the optimal scheme proposed in this paper; the2.19° skew angle scheme is designed for comparison with the classical method widely adopted in the field of motor design—"skewing by one stator slot pitch". For the 144-slot motor studied in this paper, the stator slot pitch is 2.5°. In continuous skew design, the total skew angle is typically taken as 2.5 . However, to equivalently implement this classical design in an 8-segment skewed rotor structure, the total skew angle needs to be converted to 2.5° * 7/8 ≈ 2.19°.

For the 144-slot 32-pole motor investigated in this paper, the least common multiple of the number of slots and poles is 288. Consequently, one cogging torque period corresponds to a mechanical angle of 360°/288 = 1.25° . To ensure a more accurate simulation of the cogging torque, the rotational speed of the motor is set to 1 degree per second.

The specific values of the motor's cogging torque are compared in Table 3, and its waveform is illustrated in Fig. 5.

Table 3. Cogging torque values under different skew angles

Skew angle (°)	**0**	**1.09**	**2.19**
Peak-to-peak torque (N·m)	2 666	8.6	12.08
Reduction (%)	0	99.7	99.5

This paper has been accepted for publication in the AEE journal. This is the version, which has not been fully edited and content may change prior to final publication. Citation information: DOI 10.24425/aee.2026.158267

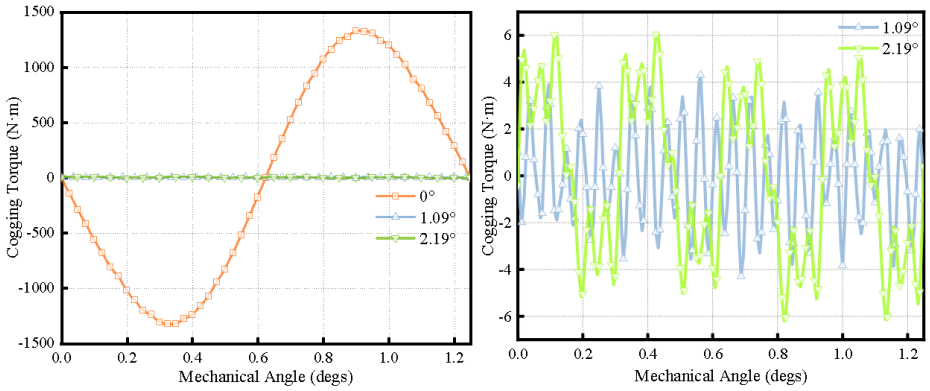

Fig. 5. Waveforms of cogging torque

Figure 6 compares the cogging torque waveforms under different skew angles obtained from the analytical calculation method and the finite element method, where subfigures (a), (b), and (c) correspond to the cases of no skew, a skew angle of 1.09°, and a skew angle of 2.19°, respectively. The comparison reveals that the waveforms from the two methods are in good agreement, with an amplitude error of less than 5%.

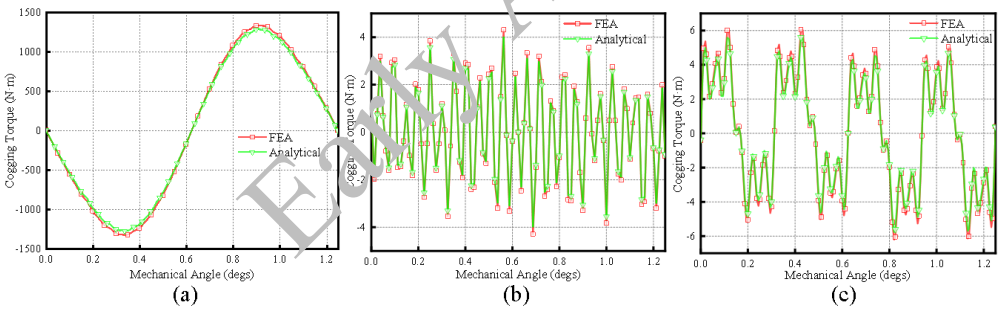

Fig. 6. (a) Skew angle: 0°; (b) skew angle: 1.09°; (c) skew angle: 2.19°

Combining the cogging torque data from Table 3, it can be observed that when the skew angle is 0°, the peak-to-peak cogging torque reaches a high value of 2 666 N·m. With a skew angle of 1.09°, the peak-to-peak cogging torque is significantly reduced to only 8.6 N·m, corresponding to a remarkable suppression of 99.7%. However, further increasing the skew angle to 2.19°results in an increase in the peak-to-peak torque to 12.08 N·m and a slight decrease in the suppression level to 99.5%. This indicates that an excessive skew angle may lead to over-modulation of the magnetic field, potentially introducing new harmonic components; thus, a larger angle is not necessarily better. This finding is consistent with the theoretical analysis in Chapter 2: when the skew angle deviates from the optimal value of 1.09°, the cancellation factor $\sin(nkzN_s\theta_{s1}/2)$ for the dominant cogging torque harmonic no longer attains its minimum, resulting in reduced suppression effectiveness. Consequently, a skew angle of 1.09° not only

This paper has been accepted for publication in the AEE journal. This is the version, which has not been fully edited and content may change prior to final publication. Citation information: DOI 10.24425/aee.2026.158267

confines the peak cogging torque to an extremely low level but also maintains the optimal degree of attenuation, making it the ideal parameter for efficient cogging torque suppression. The high degree of consistency between the results obtained from the analytical method and the finite element simulations further validates the accuracy of the calculations.

4. Analysis of electromagnetic performance

To validate the effect of different skew angles on motor performance, a comparative FEA is conducted using the three aforementioned skew schemes. Considering the motor dimensions and manufacturing constraints, an 8-segment skewed rotor configuration was adopted. The three schemes differ only in the total rotor skew angle, while all other structural and electromagnetic parameters remain identical. Based on the formula for the optimal rotor skew angle derived earlier, when the rotor is divided into 8 segments, the corresponding optimal mechanical skew angle is calculated to be 1.09° Accordingly, three motor schemes are defined: Scheme 1 employs a rotor with no skew. Scheme 2 utilizes an axially 8-segment skewed rotor with a total mechanical skew angle of 1.09°. Scheme 3 also uses an axially 8-segment skewed rotor but with a total mechanical skew angle of 2.19°, serving as a comparative case.

4.1. No-load back-EMF analysis

The no-load back-EMF is a critical indicator for evaluating the performance of permanent magnet motors. Its amplitude determines the voltage output capability of the motor, while the sinusoidal purity and harmonic content of its waveform directly influence key operational characteristics such as torque ripple and acoustic noise. Rotor skewing is an effective means of improving the air-gap magnetic field, and variations in the skew angle significantly impact the characteristics of the no-load back-EMF. Therefore, investigating the variation patterns of back-EMF under different skew angles is of great importance for optimizing the electromagnetic performance of the motor and ensuring smooth operation.

The waveforms of the motor's no-load back-EMF are shown in Fig. 7, and a comparison of specific parameters and total harmonic distortion (THD) is presented in Table 4.

This paper has been accepted for publication in the AEE journal. This is the version, which has not been fully edited and content may change prior to final publication. Citation information: DOI 10.24425/aee.2026.158267

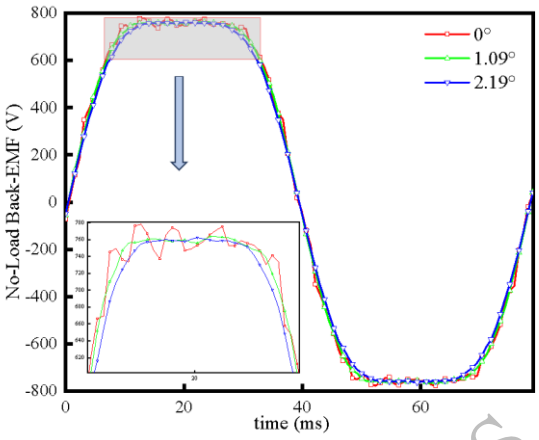

Fig. 7. No-load back-EMF waveforms

Table 4. RMS values and THD (%) of the no-load back-EMF

Skew angle (°)	**0**	**1.09**	**2.19**
RMS value (V)	642.49	638.36	626.91
Reduction in RMS (%)	0	0.64	2.42
THD (%)	17.21	16.53	14.53

The no-load back-EMF waveforms under different skew angles were subjected to Fourier decomposition. The corresponding harmonic orders and their respective amplitudes are illustrated in Fig. 8.

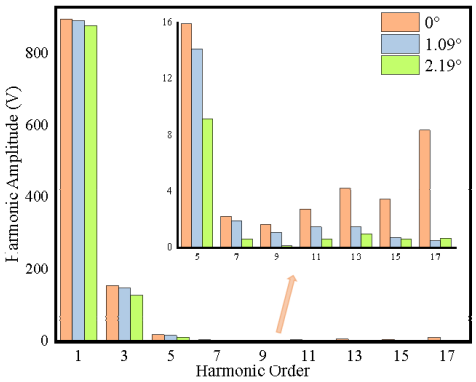

Fig. 8. Harmonic analysis of the no-load back-EMF by order

This paper has been accepted for publication in the AEE journal. This is the version, which has not been fully edited and content may change prior to final publication. Citation information: DOI 10.24425/aee.2026.158267

Figure 8 and Table 4 reveal that as the skew angle increases, both the RMS value and the THD of the no-load back-EMF decrease. When the skew angle increases from 0° to 2.19°, the no-load back-EMF RMS value decreases from 642.49 V to 626.91 V, a reduction of 2.42%. When the skew angle increases from 0° to 1.09°, the RMS value decreases from 642.49 V to 638.36 V, a marginal reduction of only 0.64%; meanwhile, the THD is also improved. The results demonstrate that adopting a 1.09° skew structure effectively suppresses harmonics and enhances no-load back-EMF waveform quality, without significantly compromising the motor's output capability, inducing only a limited attenuation in amplitude.

4.2. Electromagnetic torque analysis

Electromagnetic torque is a key metric reflecting the load-operation characteristics of permanent magnet motors. Its magnitude and ripple amplitude not only determine the effective output capability of the motor but also directly influence the stability and control precision of the drive system. Adjusting the skew angle modifies the air-gap magnetic field distribution, thereby affecting the output characteristics of the electromagnetic torque. Consequently, investigating the behavior of electromagnetic torque under different skew angles is a crucial prerequisite for achieving the co-optimization of motor structure and performance.

The electromagnetic torque waveforms of the motor are shown in Fig. 9, and a comparison of the average torque and torque ripple parameters is presented in Table 5.

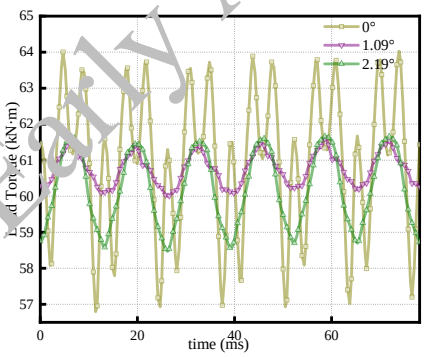

Fig. 9. Electromagnetic torque waveforms

Table 5. Load average torque and torque ripple under different skew angles

Skew angle (°)	**0**	**1.09**	**2.19**
Average torque (kN·m)	60.95	60.74	60.20
Peak-to-peak torque (kN·m)	7.14	2.01	3.60
Torque ripple (%)	11.70	3.31	5.98
Torque ripple reduction (%)	0	72.05	48.89

This paper has been accepted for publication in the AEE journal. This is the version, which has not been fully edited and content may change prior to final publication. Citation information: DOI 10.24425/aee.2026.158267

Combined with the comparative analysis of Fig. 9 and Table 5, it can be observed that as the skew angle increases, the average torque of the motor shows a gradual declining trend, while the torque ripple is significantly suppressed. When the skew angle is 1.09°, the peak-to-peak torque ripple decreases from 7.14 kN·m (without skew) to 2.01 kN·m, a reduction of 5.13 kN·m. The corresponding torque ripple percentage is merely 3.31%, representing a 72.05% suppression rate. However, when the skew angle is increased to 2.19°, the torque ripple percentage rises to 5.98%, and the suppression rate decreases to 48.9%. Comparison reveals that with a 1.09° skew, the reduction in average torque is minimal at only 0.21 kN·m (less than 0.35%), which does not affect the normal operation of the motor. At this angle, the torque ripple is minimized, achieving the optimal suppression effect.

To evaluate the influence of the skew angle on the overall motor performance from the perspective of input characteristics, the current characteristics, power factor, and efficiency of different skew schemes are compared under the same output torque of 50 kN·m ,approximately 80% of the rated load. The results are presented in Table 6.

Table 6. Influence of different skew angles on motor efficiency

Skew angle (°)	**0**	**1.09**	**2.19**
Output torque (kN·m)	50.00	50.00	50.00
Current RMS (A)	135.21	136.00	140.18
Power factor	0.9861	0.9807	0.9607
Efficiency (%)	95.20	95.16	94.25

Analysis of Table 6 indicates that with a skew angle of 1.09°, compared to the non-skewed configuration, the RMS current increases by merely 0.79 A, while the power factor and efficiency decrease by 0.55% and 0.04%, respectively. These effects are negligible. In contrast, when the skew angle is increased to 2.19°, the RMS current rises notably by 4.18 A, and the power factor and efficiency drop by 2.04% and 0.96%, respectively. In summary, the 1.09° skew scheme demonstrates optimal performance in torque ripple suppression, current characteristics, power factor, and efficiency, establishing it as the preferred choice for achieving high-performance, low-ripple motor operation.

5. Experimental verification

To validate the accuracy of the simulation model, an experimental prototype was fabricated according to the motor specifications. A photograph of the experimental prototype and its segmented skewed rotor is presented in Fig. 10.

This paper has been accepted for publication in the AEE journal. This is the version, which has not been fully edited and content may change prior to final publication. Citation information: DOI 10.24425/aee.2026.158267

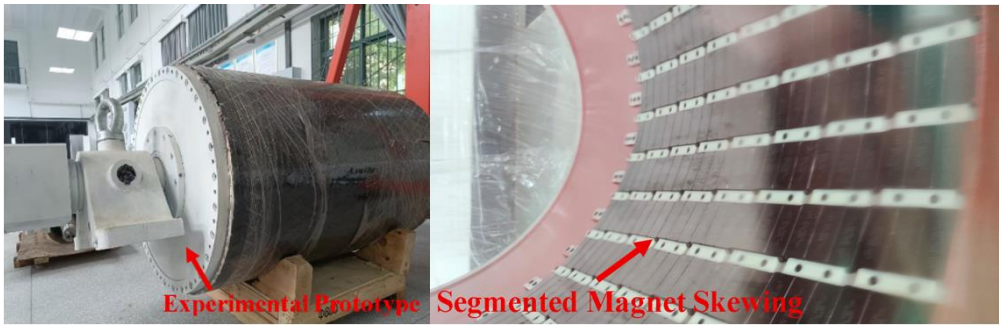

Fig. 10. Experimental prototype and a photograph of the segmented skewed rotor

A test bench was established, as shown in Fig. 11, comprising primarily a prime mover, a torque transducer, a power analyzer, and a data acquisition system. Experimental data acquisition is illustrated in Fig. 12. The tests aimed to measure the no-load back-EMF at rated speed and the load current under conditions identical to the FEA simulations, enabling a direct comparison with the simulated results to validate the model's reliability.

Fig. 11.Outer-rotor prototype test bench

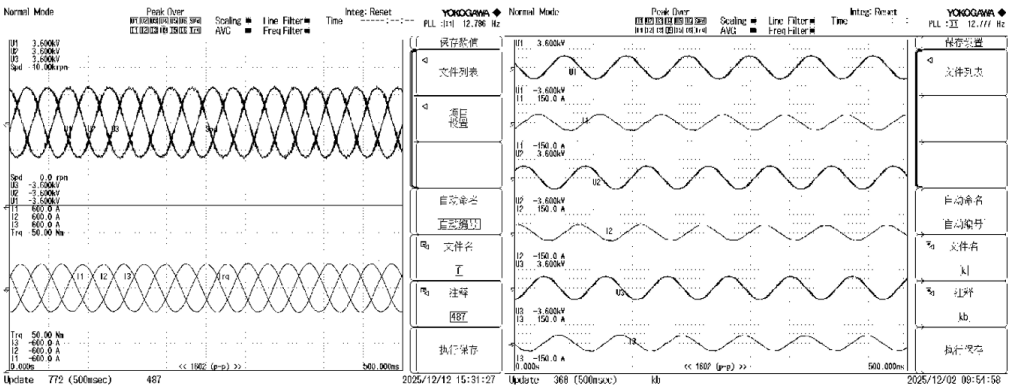

Fig. 12. Experimental data acquisition

This paper has been accepted for publication in the AEE journal. This is the version, which has not been fully edited and content may change prior to final publication. Citation information: DOI 10.24425/aee.2026.158267

To validate the accuracy of the simulation model, the prototype was driven to its rated speed by a prime mover. The line-to-line no-load back-EMF at rated speed was measured using a power analyzer. The comparison between the experimental and FEA results is shown in Fig. 13(a). Furthermore, the prototype current was measured under a 77% load condition and compared with the simulated load current, as illustrated in Fig. 13(b). The corresponding RMS values are summarized in Table 7.

Table 7. Comparison between FEA and experimental data

Comparison Item	**Experimental value**	**FEA value**	**Relative error (%)**
No-load back-EMF RMS (V)	640.8	638.36	0.38
Load current RMS (A)	126.60	127.71	0.87

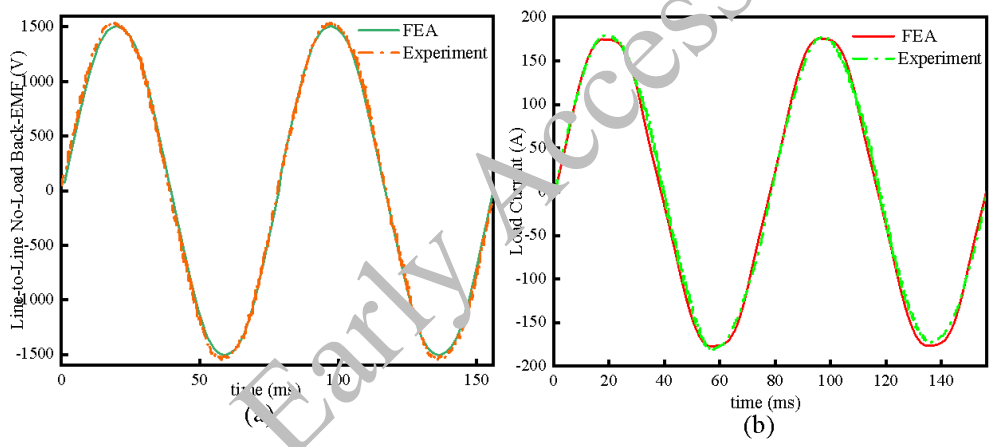

Fig. 13. (a) Line-to-line no-load back-EMF; (b) load current

Minor discrepancies exist in the no-load back-EMF and load current, with relative errors of 0.38% and 0.87%, respectively. These primarily arise from measurement system accuracy, manufacturing and assembly tolerances, and the idealized assumptions inherent in the simulation model. Overall, the results demonstrate that the established finite element model accurately captures the electromagnetic characteristics of the actual motor. This not only validates the reliability of the model itself, but also further substantiates the effectiveness of the preceding segmented skew angle optimization analysis, thereby providing credible experimental support for relevant engineering applications.

This paper has been accepted for publication in the AEE journal. This is the version, which has not been fully edited and content may change prior to final publication. Citation information: DOI 10.24425/aee.2026.158267

6. Conclusion

To address the pronounced issue of torque ripple in high-power mining ORPMMs, this paper presents an optimized design method based on segmented rotor step-skewing, systematically validated through analytical calculation, finite element simulation, and experimental testing. The main conclusions are as follows:

1. An analytical model for cogging torque is derived based on the energy method, and a calculation formula for the optimal skew angle applicable to outer-rotor motors was proposed. This angle is determined jointly by the pole-slot combination and the number of segments.

2. With an 8-segment step-skew and a skew angle of 1.09°, the peak-to-peak cogging torque was reduced from 2666 N·m to 8.6 N·m, achieving an attenuation rate of 99.7%.

3. A skew angle of 1.09°significantly improved the waveform distortion while ensuring a minimal reduction in the no-load back-EMF RMS value of only 0.64%. The load torque ripple was reduced from 11.70% to 3.31%, a suppression of 72.05% with an average torque loss of less than 0.35%.

4. The prototype test results show close agreement with the simulation data, with relative errors of 0.38% for the line-to-line no-load back-EMF RMS value and 0.87% for the load current RMS value, thereby validating the accuracy and engineering feasibility of the developed method.

References

[1] Lyskawinski W., *Comparative analysis of energy performance of squirrel cage induction motor, line-start synchronous reluctance and permanent magnet motors employing the same stator design*, Archives of Electrical Engineering, vol. 69, no. 4, pp. 967–981 (2020), DOI: 10.24425/aee.2020.134642

[2] Gan X.-G., Fan Z.-J., Li J.-C., *Analysis of electromagnetic performance of the interior permanent magnet brushless DC motor with stator slot skewed structure based on quasi-3D moving electromagnetic-field circuit coupling calculation*, Archives of Electrical Engineering, vol. 71, no. 1, pp. 159–174 (2022), DOI: 10.24425/aee.2022.140203.

[3] Chen H., EL-Refaie A.M., Zuo Y., Cai S., Cao L., Lee C.H.T., *Comparative Study and Design Optimization of a Dual-Mechanical-Port Electric Machine for Hybrid Electric Vehicle Applications*, IEEE Transactions on Vehicular Technology, vol. 71, no. 8, pp. 8341–8353 (2022), DOI: 10.1109/TVT.2022.3175476.

[4] Cheng M., Zhou J., Qian W., Wang B., Zhao C., Han P., *Advanced Electrical Motors and Control Strategies for High-quality Servo Systems - A Comprehensive Review*, Chinese Journal of Electrical Engineering, vol. 10, no. 1, pp. 63–85 (2024), DOI: 10.23919/CJEE.2023.000048

[5] Ogidi O.O., Barendse P.S., Khan M.A., *Influence of Rotor Topologies and Cogging Torque Minimization Techniques in the Detection of Static Eccentricities in Axial-Flux Permanent-Magnet Machine*, IEEE Transactions on Industry Applications, vol. 53, no. 1, pp. 161–170 (2017), DOI: 10.1109/TIA.2016.2616320.

[6] Xu M., Zhao W., Ji J., Chen Q., Liu G., *Auxiliary Notching Rotor Design to Minimize Torque Ripple for Interior Permanent Magnet Machines*, IEEE Transactions on Industrial Electronics, vol. 71, no. 10, pp. 12051–12062 (2024), DOI: 10.1109/TIE.2024.3349580.

[7] Yi P., Zheng W., Li X., *Overview of Torque Ripple Minimization Methods for Permanent Magnet Synchronous Motors Based on Harmonic Injection*, Chinese Journal of Electrical Engineering, vol. 10, no. 2, pp. 16–29 (2024), DOI: 10.23919/CJEE.2023.000045.

This paper has been accepted for publication in the AEE journal. This is the version, which has not been fully edited and content may change prior to final publication. Citation information: DOI 10.24425/aee.2026.158267

[8] Lu Y., Wang C., Huang J., *Investigation and Analysis of Cogging Torque for Axial Flux Permanent Magnet Machines*, 2024 27th International Conference on Electrical Machines and Systems (ICEMS), Fukuoka, Japan, pp. 1755–1760 (2024), DOI: 10.23919/ICEMS60997.2024.10921049.

[9] Arafat M.Y., Murshed M., Hasan M.M., Razzak M.A., *Impacts of cogging torque and its reduction for an external rotor permanent magnet alternator*, 2016 5th International Conference on Informatics, Electronics and Vision (ICIEV), Dhaka, Bangladesh, pp. 536–541 (2016), DOI: 10.1109/ICIEV.2016.7760061.

[10] Setiabudy R., Herlina W., *Investigation of the influence of variations in the number and width of anti-notch depending on cogging torque reduction*, 2016 3rd International Conference on Information Technology, Computer, and Electrical Engineering (ICITACEE), Semarang, Indonesia, pp. 164–167 (2016), DOI: 10.1109/ICITACEE.2016.7892431.

[11] Kanapara A.J., Badgujar K.P., *Performance Improvement of Permanent Magnet Brushless DC Motor through Cogging Torque Reduction Techniques*, 2020 21st National Power Systems Conference (NPSC), Gandhinagar, India, pp. 1–6 (2020), DOI: 10.1109/NPSC49263.2020.9331855.

[12] Kapil A., Satish B., *Analysis of cogging torque reduction by increasing magnet edge inset in radial flux permanent magnet brushless DC motor*, 2016 IEEE 1st International Conference on Power Electronics, Intelligent Control and Energy Systems (ICPEICES), Delhi, India, pp. 1–4 (2016), DOI: 10.1109/ICPEICES.2016.7853066.

[13] Girgin M.T., Aydin M., *Elimination of Cogging Torque for Axial Flux Permanent Magnet Motors Based on Current Harmonic Injection*, 2020 International Conference on Electrical Machines (ICEM), Gothenburg, Sweden, pp. 1117–1122 (2020), DOI: 10.1109/ICEM49940.2020.9270642.

[14] Kim R.-E., Hahn S., Seo J., *A New analysis Method Based on Lumped Magnetic Circuit Model for Surface Permanent-Magnet Machines with Step Skewed Rotor*, 2022 IEEE 20th Biennial Conference on Electromagnetic Field Computation (CEFC), Denver, CO, USA, pp. 1–2 (2022), DOI: 10.1109/CEFC55061.2022.9940697.

[15] Nian S., Zhu L., Luo X., Huang Z., *Analytical Methods for Optimal Rotor Step-Skewing To Minimize Cogging Torque in Permanent Magnet Motors*, 2019 22nd International Conference on Electrical Machines and Systems (ICEMS), Harbin, China, pp. 1–5 (2019), DOI: 10.1109/ICEMS.2019.8921502.

[16] Liu F., Wang X., Xing Z., Yu A., Li C., *Reduction of cogging torque and electromagnetic vibration based on different combination of pole arc coefficient for interior permanent magnet synchronous machine*, CES Transactions on Electrical Machines and Systems, vol. 5, no. 4, pp. 291–300 (2021), DOI: 10.30941/CESTEMS.2021.00034.

[17] Xu J., Zhao W., Wang N., Wang X., *Design and Analysis of Low-Speed High-Torque Permanent Magnet Synchronous Machines for Industrial Agitators*, 2021 24th International Conference on Electrical Machines and Systems (ICEMS), Gyeongju, Korea, pp. 1223–1227 (2021), DOI: 10.23919/ICEMS52562.2021.9634285.

[18] Huang Y., Wang D., Li Z., Tu X., Nie J., Wang X., *Electromagnetic Performance Analysis and Multi-Objective Optimal Design of A Novel Magnet-Shifted PM Motor for Reducing Torque Ripple*, 2024 IEEE 21st Biennial Conference on Electromagnetic Field Computation (CEFC), Jeju, Korea, pp. 1–2 (2024), DOI: 10.1109/CEFC61729.2024.10585644.

[19] Huang L.R., Feng J.H., Guo S.Y., Shi J.X., Chu W.Q., Zhu Z.Q., *Analysis of Torque Production in Variable Flux Reluctance Machines*, IEEE Transactions on Energy Conversion, vol. 32, no. 4, pp. 1297–1308 (2017), DOI: 10.1109/TEC.2017.2698836.

[20] Shen Y., Lu Q., Shi T., Xia C., *Analysis of Torque Production in Variable Flux Reluctance Machines*, IEEE Transactions on Industry Applications, vol. 57, no. 4, pp. 3666–3677 (2021), DOI: 10.1109/TIA.2021.3079344.

[21] Xing Z., Wang X., Zhao W., *Electromagnetic Vibration Analysis of Surface-Mounted Permanent Magnet Synchronous Machine*, 2018 IEEE International Magnetics Conference (INTERMAG), Singapore, pp. 1–1 (2018), DOI: 10.1109/INTMAG.2018.8508606.

[22] Cheng M., Xu Z., Jiang Y., Zhao C., *Investigation of Cogging Torque Generation Mechanisms in Flux-switching Permanent Magnet Machines Based on General Air-gap Field Modulation Theory*,

This paper has been accepted for publication in the AEE journal. This is the version, which has not been fully edited and content may change prior to final publication. Citation information: DOI 10.24425/aee.2026.158267

Chinese Journal of Electrical Engineering, vol. 11, no. 2, pp. 207–215 (2025), DOI: 10.23919/CJEE.2025.000135.

[23] Xiuhe Wang, *Permanent Magnet Motors 3rd ed*., China Electric Power Press (2023).

[24] Zhao J., Quan X., Tong X., Lin M., *Cogging Torque Reduction in Double-Rotor Hybrid Excited Axial Switched-Flux Permanent Magnet Machine*, IEEE Transactions on Applied Superconductivity, vol. 30, no. 4, pp. 1–5 (2020), DOI: 10.1109/TASC.2020.2965886.

[25] Li Z., Yu X., Wang X., Xing X., *Optimization and Analysis of Cogging Torque of Permanent Magnet Spherical Motor*, IEEE Transactions on Applied Superconductivity, vol. 31, no. 8, pp. 1–5 (2021), DOI: 10.1109/TASC.2021.3094445.